AIAA JOURNAL
Vol. 38, No. 11, November 2000

Generalized Characteristic Boundary Conditions for Computational Aeroacoustics

Jae Wook Kim* and Duck Joo Lee†
Korea Advanced Institute of Science and Technology, Taejon 305-701, Republic of Korea

An extended conservative formalism of the characteristic boundary conditions is presented on the basis of the generalized coordinates for practical computational aeroacoustics. The formalism is derived for solving the entire conservative form of the compressible Euler or Navier–Stokes equations on the body-fitted grid mesh system by using the high-order and high-resolution numerical schemes. It includes the matrices of transformation between the conservative and the characteristic variables, which were already derived in the literature to analyze the eigenvalue–eigenvector modes in an arbitrary direction. The conservation-form governing equations with their full terms are solved at the boundaries, and no kind of extrapolation or simplification of the equations is included in this formalism. Additional correction terms are devised to preserve the conservative form of flux derivative terms in the generalized coordinates. Especially, the soft inflow conditions are presented to keep the nonreflecting features, as well as to maintain the mean value of inflow velocity at the inlet boundary. These boundary conditions are applied to the actual computation of two-dimensional viscous cylinder flows with Reynolds number of 400 on the grid meshes clustered on the cylinder surface and the downstream region. The Strouhal number due to von Kármán vortex streets, root-mean-square lift coefficient, and mean drag coefficient are evaluated correctly in comparison with experimental data. The far-field sound pressure levels are measured directly in this computation, and the accuracy is validated by an analytic formula derived in the literature.

I. Introduction

RECENT computational aeroacoustics (CAA) or computational fluid dynamics for the compressible flows can be classified mainly into three cases: 1) unsteady free shear or jet flow, 2) steady or unsteady flow around a solid body, and 3) scattering of acoustic waves over a solid body without mean flow. Case 1 uses uniform or nonuniform rectangular grid meshes and time-dependent far-field boundary conditions without a solid body in the flow. Case 2 uses body-fitted grid meshes in generalized coordinates and simple boundary conditions for surface pressure, where the major interests are the flows over the surface, not the far-field acoustic pressure. Case 3 uses linearized governing equations with high-order schemes and time-dependent boundary conditions for the body and the far field, where the acoustic sources are given, not generated. Many kinds of numerical algorithms and boundary conditions have been developed for each case with their own original contributions, but these are confined to the limit conditions as mentioned earlier. The ultimate purpose is to achieve a general algorithm and solver for direct computation of both the flow near a solid body and the acoustic waves in far field, which is able to cover all three cases. This kind of work has not yet been accomplished, in spite of many previous attempts. Some difficulties in approaching this goal appear in the presence of a solid body that requires special treatments to the boundary conditions for the surface and the far field on the body-fitted grid meshes in the generalized coordinates.

In this study, it is realized that there are three essential parts to satisfy the purpose, 1) the high-order and high-resolution schemes in both space and time, 2) entire conservation-form governing equations on the body-fitted grid meshes in the generalized coordinates (conservation form means all of the spatial variables including transformation metrics and Jacobians are contained in the differential operator), and 3) accurate time-dependent boundary conditions to solve the entire conservation-form governing equations at the body surface and the far-field plane including soft (nonreflecting) inflow conditions in the presence of a solid body as a acoustic generator.[1] Part 1 is used for accurate and precise evaluations of the spatial derivatives and the temporal integrals, which require more computation time than the other standard schemes. Part 2 has an important meaning, especially when the target problem includes nonlinear discontinuous waves, because the nonlinear flow properties at the near field become effective dipole or quadrupole sources of sound at the far field as Mach number increases. (Usually, the nonconservation-form equations produce well-known errors in phase speeds or locations of the nonlinear waves, as have been reported in the literature.) Moreover, part 2 demands much less computation time for differencing operations than in the case of using part 1 because the numbers of spatial derivative terms of the entire conservation-form equations are one-half times in two dimensions and one-third times in three dimensions as many as those of the nonconservation-form equations, in the generalized coordinates. Therefore, part 2 has advantages in nonlinearity and efficiency at the same time. Part 3 is the focus of this paper. The authors choose the characteristic boundary conditions to meet part 3 because these can be used for both the solid body and the far field, do not require any linearization or asymptotic analysis, and especially can work well with part 2. Especially the soft (nonreflecting) inflow conditions are very critical in the case of flow around a solid body. Some numerical errors in the presence of a solid body can contaminate the flowfield rapidly because the dipole source of the solid body is much stronger than the quadrupole source of a pure jet or shear flow in the subsonic range. This paper presents a generalized formalism of the characteristic boundary conditions including the soft inflow conditions for the solutions of entire conservation-form governing equations, to satisfy parts 2 and 3 at the same time and to accomplish the ultimate purpose mentioned earlier.

Recently, several kinds of numerical boundary conditions that are physically precise and correct have been proposed for the unsteady CAA. These proposals can be classified in several categories,[2,3] namely, the quasi-one-dimensional characteristics,[4–6] the decomposition of solutions into Fourier modes,[7] the asymptotic analysis of governing equations from a large distance,[8–10] the perfectly matched layer technique,[11,12] and the artificial boundary conditions.[13,14] As for the characteristic boundary conditions, Thompson[4,5] decomposed hyperbolic equations into wave modes of definite velocity and then specified the characteristic boundary conditions for incoming

---

Received 14 October 1999; revision received 17 May 2000; accepted for publication 18 May 2000.

*Graduate Student, Department of Aerospace Engineering, 373-1 Kusong-dong, Yusong-gu; currently Postdoctoral Research Assistant, Department of Aerospace Engineering, Pennsylvania State University, University Park, PA 16802.

†Professor, Department of Aerospace Engineering, 373-1 Kusong-dong, Yusong-gu. Member AIAA.

waves. The starting point of his analysis was the nonlinear Euler equations. The idea of his approach was that one-dimensional characteristic analysis could be performed by consideration of the transverse terms as a constant source term. The amplitudes of outward propagating waves are defined entirely from the variables inside computational domain, whereas those of inward propagating waves are specified as the characteristic boundary conditions. This approach includes no linearization procedure and is not intended for idealized model problems. Thus, these kinds of boundary conditions can be applied to both linear and nonlinear problems at the same time. The characteristic boundary conditions were utilized and developed by Poinsot and Lele[6] for the Navier–Stokes computations with the low-dissipation and low-dispersion algorithms. These were still based on the local one-dimensional inviscid analysis, which has remained a defect of the characteristic boundary conditions with the lack of true multidimensionality. The challenge remains to get rid of this kind of defect. Recently Lockhard and Morris[15] introduced a possible way to improve the multidimensionality of the characteristic boundary conditions at the slip wall.

The variations of characteristic boundary conditions have been used for the past two decades in problems and research areas.[3–6] However, thus far no one has presented a conservative formulation of the characteristic boundary conditions derived on the basis of generalized coordinates for the nonuniform body-fitted grid meshes, even though those calculations were made in generalized coordinates with a solid body, which was done possibly by the nonconservative form obtained directly from a simple coordinate transformation using the chain rule. Moreover, each of those works was confined to only one of the three cases (1–3) described at the beginning of this section, and therefore it was impossible to calculate both the near-field flow fluctuations and the far-field acoustic waves at the same time. This paper is devoted to overcome this limitation for CAA and to suggest an improved algorithm that is able to cover all three cases.

In the present paper, the generalized characteristic boundary conditions are proposed for practical CAA on nonuniform body-fitted grid meshes. Extended conservative formulations are derived in the generalized coordinates for solving the entire conservation-form Euler or Navier–Stokes equations using high-order and high-resolution numerical schemes. In this approach, the additional correction terms are devised to preserve the conservative form of the flux derivative terms in the generalized coordinates. The meaning and importance of the conservative form in the generalized coordinates has already been emphasized earlier. This paper presents the conservative formalism of the generalized characteristic boundary conditions for the first time, among the many publications about the characteristic boundary conditions. Thus its derivation procedure is neither straightforward nor simple, and it will be a guide for many users of the characteristic boundary conditions.

In particular, this paper presents the soft inflow conditions for CAA in the presence of a solid body. Usually, the velocity or mass flux and the temperature have been fixed by a constant value or prescribed by some functions at the inlet boundary, as suggested by Thompson,[4,5] Poinsot and Lele,[6] and most previous publications. This kind of condition cannot keep up with the acoustic waves propagating upstream and passing through the inlet boundary. Moreover, nonphysical disturbances at the inlet boundary can eventually contaminate the whole acoustic field, especially in the presence of a solid body, because the interaction between the inflow disturbances and the body surface can generate an efficient dipole noise source. This kind of trouble can be overcome by introducing the soft inflow conditions, and the sound pressure level can be calculated accurately at the inlet boundary as well as at the exit boundary, which is illustrated by the computation results in this paper.

The need for accurate and efficient numerical algorithms of high order and high resolution has been increased for CAA because these are able to simulate the generation and propagation of high wave number (or high-frequency) and small-amplitude wave components directly. These are almost nondissipative and much less dispersive than the standard low-order ones that have been used widely so far. By using high-order and high-resolution numerical algorithms, the boundary conditions developed in this paper are applied to an actual computation. The target problem is two-dimensional viscous cylinder flow of $Re_\infty = 400$ and $M_\infty = 0.3$, which generates the well-known von Kármán vortex streets. The nondimensional frequency (Strouhal number) of shedding vortices, the rms lift coefficient, and the mean drag coefficient are evaluated and compared with the previous experimental data. Far-field acoustic pressures induced by the dipole sound source are measured directly in this computation, and their overall sound pressure levels are compared with the analytic estimations provided by the literature. Feasibility and accuracy of the generalized characteristic boundary conditions including the soft inflow conditions are investigated and tested for further practical CAA with the high-order and high-resolution schemes.

II. Generalized Formulation

A. Transformation to Characteristic Form

The conservation-form Navier–Stokes equations in Cartesian coordinates can be decomposed into locally one-dimensional wave modes. This can be done by use of flux-Jacobian and transformation matrices between the conservative and the characteristic variables, which had been derived to analyze Euler equations through eigenvalue–eigenvector modes in an arbitrary direction. These matrices are already derived in Refs. 16 and 17 and used for the development of generalized characteristic boundary conditions in the present paper. The three-dimensional conservation-form Navier–Stokes equations can be represented in Cartesian coordinates as

$$\frac{\partial \boldsymbol{Q}}{\partial t} + \frac{\partial \boldsymbol{E}}{\partial x} + \frac{\partial \boldsymbol{F}}{\partial y} + \frac{\partial \boldsymbol{G}}{\partial z} = \boldsymbol{S}_V \tag{1}$$

where the conservative variables and the inviscid flux vectors are given as

$$\boldsymbol{Q} = [\rho, \rho u, \rho v, \rho w, \rho e_t]^T$$

$$\boldsymbol{E} = \left[\rho u, \rho u^2 + p, \rho v u, \rho w u, (\rho e_t + p)u\right]^T$$

$$\boldsymbol{F} = \left[\rho v, \rho u v, \rho v^2 + p, \rho w v, (\rho e_t + p)v\right]^T$$

$$\boldsymbol{G} = \left[\rho w, \rho u w, \rho v w, \rho w^2 + p, (\rho e_t + p)w\right]^T$$

and $\boldsymbol{S}_V$ is a source term that consists of the viscous flux derivative terms represented as

$$\boldsymbol{S}_V = \frac{\partial \boldsymbol{E}_V}{\partial x} + \frac{\partial \boldsymbol{F}_V}{\partial y} + \frac{\partial \boldsymbol{G}_V}{\partial z}$$

where the viscous flux vectors, the stress tensor components, and the heat fluxes are given as

$$\boldsymbol{E}_V = \lfloor 0, \tau_{xx}, \tau_{xy}, \tau_{xz}, u\tau_{xx} + v\tau_{xy} + w\tau_{xz} + q_x \rfloor^T$$

$$\boldsymbol{F}_V = \lfloor 0, \tau_{yx}, \tau_{yy}, \tau_{yz}, u\tau_{yx} + v\tau_{yy} + w\tau_{yz} + q_y \rfloor^T$$

$$\boldsymbol{G}_V = \lfloor 0, \tau_{zx}, \tau_{zy}, \tau_{zz}, u\tau_{zx} + v\tau_{zy} + w\tau_{zz} + q_z \rfloor^T$$

$$\tau_{xx} = \frac{1}{Re_\infty}\left(2\mu\frac{\partial u}{\partial x} + \lambda\nabla\cdot\boldsymbol{V}\right)$$

$$\tau_{yy} = \frac{1}{Re_\infty}\left(2\mu\frac{\partial v}{\partial y} + \lambda\nabla\cdot\boldsymbol{V}\right)$$

$$\tau_{zz} = \frac{1}{Re_\infty}\left(2\mu\frac{\partial w}{\partial z} + \lambda\nabla\cdot\boldsymbol{V}\right)$$

$$\tau_{xy} = \tau_{yx} = \frac{\mu}{Re_\infty}\left(\frac{\partial u}{\partial y} + \frac{\partial v}{\partial x}\right)$$

$$\tau_{yz} = \tau_{zy} = \frac{\mu}{Re_\infty}\left(\frac{\partial v}{\partial z} + \frac{\partial w}{\partial y}\right)$$

$$\tau_{zx} = \tau_{xz} = \frac{\mu}{Re_\infty}\left(\frac{\partial w}{\partial x} + \frac{\partial u}{\partial z}\right)$$

$$q_x = \frac{\mu}{(\gamma - 1)PrRe_\infty M_\infty^2}\frac{\partial T}{\partial x}$$

$$q_y = \frac{\mu}{(\gamma - 1)PrRe_\infty M_\infty^2}\frac{\partial T}{\partial y}$$

$$q_z = \frac{\mu}{(\gamma - 1)PrRe_\infty M_\infty^2}\frac{\partial T}{\partial z}$$

The starting point of analysis for the development of boundary conditions is Eq. (1). This equation is simply transformed to the nonconservation-form equation in generalized coordinates by the chain rule, and the resulting equation is

$$\frac{\partial \boldsymbol{Q}}{\partial t} + \left(\xi_x\frac{\partial \boldsymbol{E}}{\partial \xi} + \xi_y\frac{\partial \boldsymbol{F}}{\partial \xi} + \xi_z\frac{\partial \boldsymbol{G}}{\partial \xi}\right) + \left(\eta_x\frac{\partial \boldsymbol{E}}{\partial \eta} + \eta_y\frac{\partial \boldsymbol{F}}{\partial \eta} + \eta_x\frac{\partial \boldsymbol{G}}{\partial \eta}\right) + \left(\zeta_x\frac{\partial \boldsymbol{E}}{\partial \zeta} + \zeta_y\frac{\partial \boldsymbol{F}}{\partial \zeta} + \zeta_z\frac{\partial \boldsymbol{G}}{\partial \zeta}\right) = \boldsymbol{S}_V \tag{2}$$

Equation (2) can be transformed into a characteristic form in the direction normal to the computational boundary surface where ξ keeps a constant value and the resulting quasi-linear characteristic wave equation is obtained as

$$\frac{\partial \boldsymbol{R}}{\partial t} + \underline{\Lambda}\frac{\partial \boldsymbol{R}}{\partial \xi} = -\underline{\boldsymbol{P}}^{-1}\boldsymbol{S}_V^* \tag{3}$$

where the underscore means matrix. Equation (3) focuses only on the fluxes in the normal direction, whereas the transverse fluxes are considered as a source term. Then the newly defined source term is

$$\boldsymbol{S}_V^* = \boldsymbol{S}_V - \left(\eta_x\frac{\partial \boldsymbol{E}}{\partial \eta} + \eta_y\frac{\partial \boldsymbol{F}}{\partial \eta} + \eta_x\frac{\partial \boldsymbol{G}}{\partial \eta}\right) - \left(\zeta_x\frac{\partial \boldsymbol{E}}{\partial \zeta} + \zeta_y\frac{\partial \boldsymbol{F}}{\partial \zeta} + \zeta_z\frac{\partial \boldsymbol{G}}{\partial \zeta}\right)$$

The characteristic variables and the eigenvalues are represented as

$$\delta\boldsymbol{R} = \underline{\boldsymbol{P}}^{-1}\delta\boldsymbol{Q} = [\delta\rho - (1/c^2)\delta p, \delta\tilde{W}, \delta\tilde{V}, (1/\rho c)\delta p + \delta\tilde{U}, (1/\rho c)\delta p - \delta\tilde{U}]^T$$

$$\underline{\Lambda}\ \text{(diagonal)} = \left[U, U, U, U + c\sqrt{\xi_x^2 + \xi_y^2 + \xi_z^2}, U - c\sqrt{\xi_x^2 + \xi_y^2 + \xi_z^2}\right]^T$$

where c is the speed of sound. The normal (contravariant) velocity and its differential are given as

$$U = \xi_x u + \xi_y v + \xi_z w, \qquad \delta\tilde{U} = \tilde{\xi}_x\delta u + \tilde{\xi}_y\delta v + \tilde{\xi}_z\delta w$$

and the velocity differentials in the direction parallel to the boundary surface are given as

$$\delta\tilde{V} = -\tilde{\xi}_x\delta v + \tilde{\xi}_y\delta u, \qquad \delta\tilde{W} = \tilde{\xi}_x\delta w - \tilde{\xi}_z\delta u$$

The transformation matrix from the characteristic to the conservative variables and its inverse matrix can diagonalize the flux-Jacobian matrices in an arbitrary direction, and the resulting diagonal terms become the eigenvalues. These matrices and the diagonalization procedure are expressed precisely in Refs. 16 and 17. The transformation matrix from the conservative to the characteristic variables and its constituting variables is

$$\underline{\boldsymbol{P}}^{-1} = \begin{bmatrix} \boldsymbol{B}_o\cdot\boldsymbol{l}_x & (\gamma-1)\frac{u}{c^2}\tilde{\xi}_x & (\gamma-1)\frac{v}{c^2}\tilde{\xi}_x + \frac{\tilde{\xi}_z}{\rho} & (\gamma-1)\frac{w}{c^2}\tilde{\xi}_x - \frac{\tilde{\xi}_y}{\rho} & -\frac{\gamma-1}{c^2}\tilde{\xi}_x \\ \boldsymbol{B}_o\cdot\boldsymbol{l}_y & (\gamma-1)\frac{u}{c^2}\tilde{\xi}_y - \frac{\tilde{\xi}_z}{\rho} & (\gamma-1)\frac{v}{c^2}\tilde{\xi}_y & (\gamma-1)\frac{w}{c^2}\tilde{\xi}_y + \frac{\tilde{\xi}_x}{\rho} & -\frac{\gamma-1}{c^2}\tilde{\xi}_y \\ \boldsymbol{B}_o\cdot\boldsymbol{l}_z & (\gamma-1)\frac{u}{c^2}\tilde{\xi}_z + \frac{\tilde{\xi}_y}{\rho} & (\gamma-1)\frac{v}{c^2}\tilde{\xi}_z - \frac{\tilde{\xi}_x}{\rho} & (\gamma-1)\frac{w}{c^2}\tilde{\xi}_z & -\frac{\gamma-1}{c^2}\tilde{\xi}_z \\ \frac{c}{\rho}\left(\frac{\gamma-1}{2}M^2 - \frac{\boldsymbol{v}\cdot\boldsymbol{l}_\xi}{c}\right) & \boldsymbol{C}_+\cdot\boldsymbol{l}_x & \boldsymbol{C}_+\cdot\boldsymbol{l}_y & \boldsymbol{C}_+\cdot\boldsymbol{l}_z & \frac{\gamma-1}{\rho c} \\ \frac{c}{\rho}\left(\frac{\gamma-1}{2}M^2 + \frac{\boldsymbol{v}\cdot\boldsymbol{l}_\xi}{c}\right) & \boldsymbol{C}_-\cdot\boldsymbol{l}_x & \boldsymbol{C}_-\cdot\boldsymbol{l}_y & \boldsymbol{C}_-\cdot\boldsymbol{l}_z & \frac{\gamma-1}{\rho c} \end{bmatrix}$$

$$\boldsymbol{B}_o = \{1 - [(\gamma-1)/2]M^2\}\boldsymbol{l}_\xi - (1/\rho)(\boldsymbol{v}\times\boldsymbol{l}_\xi), \qquad \boldsymbol{C}_\pm = \pm(\boldsymbol{l}_\xi/\rho) - [(\gamma-1)/\rho c]\boldsymbol{v}$$

where the unit vector in the direction normal to the boundary and x-, y-, and z-direction unit vectors are given as follows:

$$\boldsymbol{l}_\xi = (\tilde{\xi}_x, \tilde{\xi}_y, \tilde{\xi}_z) = \left(1\Big/\sqrt{\xi_x^2 + \xi_y^2 + \xi_z^2}\right)(\xi_x, \xi_y, \xi_z)$$

$$\boldsymbol{l}_x = (1, 0, 0), \qquad \boldsymbol{l}_y = (0, 1, 0), \qquad \boldsymbol{l}_z = (0, 0, 1)$$

B. Analysis of Local One-Dimensional Wave Modes and Transformation to Conservative Form

Characteristic boundary conditions start from Eq. (3). An incoming convection term in the quasi-one-dimensional wave equation (3) should be determined by the other outgoing terms according to proper physical boundary conditions. Without physical boundary conditions, the incoming waves at the boundary surface have no meaning because there is no known information outside the computational domain. If one defines another expression for the convection terms as

$$L_i = \lambda_i\frac{\partial R_i}{\partial \xi} \qquad (i = 1, 2, \ldots, 5) \tag{4}$$

then the values of incoming L_i are determined by those of outgoing terms according to the soft inflow, the nonreflecting outflow or the wall conditions, where the incoming and the outgoing terms are distinguished by their eigenvalues, that is, the convection velocities. After this kind of treatment, the convection terms in Eq. (3) are transformed to the flux derivative terms in Eq. (2) by using the following relation:

$$\xi_x\frac{\partial \boldsymbol{E}}{\partial \xi} + \xi_y\frac{\partial \boldsymbol{F}}{\partial \xi} + \xi_z\frac{\partial \boldsymbol{G}}{\partial \xi} = \underline{\boldsymbol{P}}\underline{\Lambda}\frac{\partial \boldsymbol{R}}{\partial \xi} = \underline{\boldsymbol{P}}\boldsymbol{L} \tag{5}$$

where the transformation matrix from the characteristic to the conservative variables and its constituting variables are

$$\underline{\boldsymbol{P}} = \begin{bmatrix} \tilde{\xi}_x & \tilde{\xi}_y & \tilde{\xi}_z & \rho/2c & \rho/2c \\ u\tilde{\xi}_x & u\tilde{\xi}_y - \rho\tilde{\xi}_z & u\tilde{\xi}_z + \rho\tilde{\xi}_y & (\rho/2c)(u + \tilde{\xi}_x c) & (\rho/2c)(u - \tilde{\xi}_x c) \\ v\tilde{\xi}_x + \rho\tilde{\xi}_z & v\tilde{\xi}_y & v\tilde{\xi}_z - \rho\tilde{\xi}_x & (\rho/2c)(v + \tilde{\xi}_y c) & (\rho/2c)(v - \tilde{\xi}_y c) \\ w\tilde{\xi}_x - \rho\tilde{\xi}_y & w\tilde{\xi}_y + \rho\tilde{\xi}_x & w\tilde{\xi}_z & (\rho/2c)(w + \tilde{\xi}_z c) & (\rho/2c)(w - \tilde{\xi}_z c) \\ \boldsymbol{b}\cdot\boldsymbol{l}_x & \boldsymbol{b}\cdot\boldsymbol{l}_y & \boldsymbol{b}\cdot\boldsymbol{l}_z & (\rho/2c)(H + c\boldsymbol{v}\cdot\boldsymbol{l}_\xi) & (\rho/2c)(H - c\boldsymbol{v}\cdot\boldsymbol{l}_\xi) \end{bmatrix}$$

$$\boldsymbol{b} = (|\boldsymbol{v}|^2/2)\boldsymbol{l}_\xi + \rho(\boldsymbol{v}\times\boldsymbol{l}_\xi), \qquad H = |\boldsymbol{v}|^2/2 + c^2/(\gamma - 1)$$

C. Implementation Procedures for Conservation Form in Generalized Coordinates

Usually the governing equations are solved in the generalized coordinates for practical problems with boundaries such as curved surfaces or bent corners with arbitrary turning angle. Even without such boundaries, the generalized equations should be used when the grid mesh is nonuniform or clustered near some positions. The conservation-form Navier–Stokes equations can be derived in the generalized coordinates after some mathematics from Eq. (2), and these can be represented as

$$\frac{\partial\hat{\boldsymbol{Q}}}{\partial t} + \frac{\partial\hat{\boldsymbol{E}}}{\partial\xi} + \frac{\partial\hat{\boldsymbol{F}}}{\partial\eta} + \frac{\partial\hat{\boldsymbol{G}}}{\partial\zeta} = \hat{\boldsymbol{S}}_V \tag{6}$$

where the inviscid flux vectors in the generalized coordinates are given as

$$\hat{\boldsymbol{Q}} = \boldsymbol{Q}/J, \qquad \hat{\boldsymbol{E}} = (1/J)(\xi_x\boldsymbol{E} + \xi_y\boldsymbol{F} + \xi_z\boldsymbol{G})$$

$$\hat{\boldsymbol{F}} = (1/J)(\eta_x\boldsymbol{E} + \eta_y\boldsymbol{F} + \eta_z\boldsymbol{G}), \qquad \hat{\boldsymbol{G}} = (1/J)(\zeta_x\boldsymbol{E} + \zeta_y\boldsymbol{F} + \zeta_z\boldsymbol{G})$$

and $\hat{\boldsymbol{S}}_V$ is a source term that consists of the viscous flux derivative terms in the generalized coordinates, which is represented as

$$\hat{\boldsymbol{S}}_V = \frac{\partial\hat{\boldsymbol{E}}_V}{\partial\xi} + \frac{\partial\hat{\boldsymbol{F}}_V}{\partial\eta} + \frac{\partial\hat{\boldsymbol{G}}_V}{\partial\zeta}$$

where the viscous flux vectors in the generalized coordinates are as follows:

$$\hat{\boldsymbol{E}}_V = (1/J)(\xi_x\boldsymbol{E}_V + \xi_y\boldsymbol{F}_V + \xi_z\boldsymbol{G}_V)$$

$$\hat{\boldsymbol{F}}_V = (1/J)(\eta_x\boldsymbol{E}_V + \eta_y\boldsymbol{F}_V + \eta_z\boldsymbol{G}_V)$$

$$\hat{\boldsymbol{G}}_V = (1/J)(\zeta_x\boldsymbol{E}_V + \zeta_y\boldsymbol{F}_V + \zeta_z\boldsymbol{G}_V)$$

At the computational boundary, where ξ keeps a constant value, the second term in Eq. (6), which is a conservation-form normal-flux derivative term in the ξ direction, should be corrected with the physical boundary conditions. In the first step, it is simply evaluated by numerical methods such as finite difference schemes and then it is transformed to the characteristic convection term to implement physical boundary conditions in the wave modes. The relation between the conservation-form normal-flux derivative term and the characteristic convection term is given as

$$\boldsymbol{L} = \underline{\boldsymbol{P}}^{-1}J\left\{\frac{\partial\hat{\boldsymbol{E}}}{\partial\xi} - \left[\boldsymbol{E}\frac{\partial}{\partial\xi}\left(\frac{\xi_x}{J}\right) + \boldsymbol{F}\frac{\partial}{\partial\xi}\left(\frac{\xi_y}{J}\right) + \boldsymbol{G}\frac{\partial}{\partial\xi}\left(\frac{\xi_z}{J}\right)\right]\right\} \tag{7}$$

In the next step, the physical boundary conditions are imposed on the characteristic convection term $\boldsymbol{L}$, where the incoming components of $\boldsymbol{L}$ are recalculated by the other outgoing ones. In this way, newly updated $\boldsymbol{L}^*$ is obtained. Finally, the conservation-form normal-flux derivative term can be precisely corrected with the following relation:

$$\left(\frac{\partial\hat{\boldsymbol{E}}}{\partial\xi}\right)^* = \frac{1}{J}\underline{\boldsymbol{P}}\boldsymbol{L}^* + \left[\boldsymbol{E}\frac{\partial}{\partial\xi}\left(\frac{\xi_x}{J}\right) + \boldsymbol{F}\frac{\partial}{\partial\xi}\left(\frac{\xi_y}{J}\right) + \boldsymbol{G}\frac{\partial}{\partial\xi}\left(\frac{\xi_z}{J}\right)\right] \tag{8}$$

Equation (8) is the same as Eq. (7). However, one is used for correction of the characteristic convection term and the other for recalculation of the resulting normal-flux derivative term. The additional terms in the square bracket are newly devised to preserve the conservative form of the governing equations in the generalized coordinates.

D. Local One-Dimensional Inviscid Relations

At each point of the boundary, the local one-dimensional inviscid (LODI) system can be obtained by considering the wave equation (3) and neglecting its source term that contains transverse and viscous derivatives. The resulting equations are easy to interpret and allow us to infer values for the wave amplitude variations by considering the flow locally as inviscid and one dimensional. The relations obtained by this idea are not the physical conditions exactly, but should be viewed as compatibility relations between the choices made for the physical boundary conditions and the amplitudes of waves crossing the boundary.[6]

The LODI system can be cast in many different forms, depending on the choice of variables.[6] In terms of the primitive variables, the LODI system is represented as follows:

$$\frac{\partial\rho}{\partial t} + L_1 + \frac{\rho}{2c}(L_4 + L_5) = 0 \tag{9}$$

$$\frac{\partial p}{\partial t} + \frac{\rho c}{2}(L_4 + L_5) = 0 \tag{10}$$

$$\frac{\partial\tilde{W}}{\partial t} + L_2 = 0 \tag{11}$$

$$\frac{\partial\tilde{V}}{\partial t} + L_3 = 0 \tag{12}$$

$$\frac{\partial\tilde{U}}{\partial t} + \frac{1}{2}(L_4 - L_5) = 0 \tag{13}$$

Values obtained for the wave amplitude variations through LODI relations will be approximate because the complete Navier–Stokes equations involve transverse and viscous terms. Recall, however, that the boundary variables will be advanced in time using the system of Eq. (6), and thus the transverse and the viscous terms will effectively be taken into account at this stage. The LODI relations are used only to estimate the incoming wave amplitude variations. However, it seems obvious that the characteristic boundary conditions based on the LODI relations have a limitation in considering multidimensional interactions of the waves, so far. The approximation at this level can be tolerated as long as the physics of the boundary conditions are correct in the system. As reported in the literature, the crisis arises when strong vortices, that is, the compact sources of oblique vorticity waves, pass through the boundary in the case of high-speed jet or shear flows, where the LODI relations makes serious acoustic reflections without proper treatments.[2,3,6] Attempts should be made to get beyond the LODI approximations and to approach the true multidimensionality in the future.

III. Practical Implementation

In this section, more detail of the generalized characteristic boundary conditions is given by presenting examples of practical implementation. The physical properties of the boundary are included, and therefore, the examples are classified according to physical conditions. The soft (nonreflecting) inflow conditions will be given more attention because these raise additional difficulties as explained in the Introduction. The examples are presented in the following subsections.

A. Soft Inflow Conditions

Many sets of physical boundary conditions can be considered on a subsonic inlet boundary. As an example, one can choose a case where some primitive variables are imposed by a predetermined function on it. For example, Poinsot and Lele[6] prescribed the velocity and the temperature by fixed functions or the freestream values at the inlet boundary. This case, however, will be physically incorrect and gives wrong results from the aeroacoustic point of view because the inlet plane $\xi = 0$ is a hard boundary and nonphysical wave reflections can be produced on it. It is proper to fix the primitive variables only when the inflow is supersonic. Therefore, soft boundary conditions are needed for physically correct aeroacoustic solutions on the subsonic inlet boundary. Typical nonreflecting conditions can be used as the soft inflow boundary conditions, but these may decrease the inflow velocity as compression waves pass through the inlet plane and cannot maintain the desired inflow states, which becomes more significant when a solid body is located in the flow. The soft inflow conditions with nonreflective features and maintaining the mean amplitude of the inflow velocity are considered here. For a three-dimensional subsonic flow, four characteristic waves, L_1, L_2, L_3, and L_4 are entering the computational domain while one wave L_5 is leaving it at the speed of λ_5. To advance the solution in time on the boundary, it is necessary to determine the amplitudes L_i of the different waves crossing the boundary. Only one of these waves, L_5, can be computed from interior node points, and the others are determined by the soft inflow conditions.

One special physical condition is chosen for the soft inflow conditions in this paper; that is, far upstream velocity and pressure are imposed. Moreover, when the inlet plane is located in the far field from disturbances, one can consider the inflow isentropic if viewed in the direction normal to the boundary, and a quasi-isentropic condition can be imposed on it. These conditions do not fix any components of the primitive variables; thus all of the equations in the system of Eq. (6) should be solved at the boundary. The condition of far upstream velocity and pressure specified is now used to obtain the amplitude variations of the incoming waves L_2, L_3, and L_4. The quasi-isentropic condition is for another incoming wave L_1. The outgoing wave L_5 is computed from interior points using Eq. (7).

If the inlet velocity and pressure are not close to those in far upstream, reflected waves will enter the domain through the inlet boundary to bring the mean inlet velocity and pressure back, close to the far upstream value. A simple way to ensure a well-posed state is to set the amplitude of the incoming wave as

$$L_2 = K_{\mathrm{in}}[(\tilde{W} - \tilde{W}_\infty)/2] = K_{\mathrm{in}}\{[\tilde{\xi}_x(w - w_\infty) - \tilde{\xi}_z(u - u_\infty)]/2\} \tag{14}$$

$$L_3 = K_{\mathrm{in}}[(\tilde{V} - \tilde{V}_\infty)/2] = K_{\mathrm{in}}\{[-\tilde{\xi}_x(v - v_\infty) + \tilde{\xi}_y(u - u_\infty)]/2\} \tag{15}$$

$$\begin{aligned} L_4 &= K_{\mathrm{in}}[(\tilde{U} - \tilde{U}_\infty) + (p - p_\infty)/\rho c] \\ &= K_{\mathrm{in}}[\tilde{\xi}_x(u - u_\infty) + \tilde{\xi}_y(v - v_\infty) + \tilde{\xi}_z(w - w_\infty) \\ &\quad + (p - p_\infty)/\rho c] \end{aligned} \tag{16}$$

where K_{in} is a constant expressed as

$$K_{\mathrm{in}} = \sigma_{\mathrm{in}}\left(1 - M_{\max}^2\right)(c/l) \tag{17}$$

where σ_{in} is a coefficient to control the partial reflectivity at the inlet boundary, $M_{\max}$ is the maximum Mach number in the flow, and l is a characteristic length of the domain. Equations (14–17) are similar to those for the nonreflecting outflow conditions proposed in Ref. 6, where the value of $\sigma_{\mathrm{out}} = 0.25$ was used. The authors examined the influence of the parameter σ_{in} on the present computation and validated that identically correct results were obtained when it was bounded in the range of 0.1–0.4. The effect of drifting mean pressure level appeared for values out of this range. The value of $\sigma_{\mathrm{in}} = 0.25$ is recommended also for the soft inflow conditions in this paper. It turns out that the application of the soft inflow conditions to actual computations gives satisfactory results; that is, the mean amplitude of the inflow velocity is maintained and the nonreflection effect is achieved at the same time.

The quasi-isentropic condition sets the value of another incoming wave $L_1 = 0$, where L_1 is the amplitude of the entropy wave as expressed in Sec. II.A. In this procedure, therefore, all amplitudes of the characteristic waves are determined, and the results are inserted in Eq. (8) to impose the soft inflow boundary conditions on the normal-flux derivative terms of Eq. (6). Not only the quasi-isentropic condition suggested here, but also constant temperature or total-enthalpy condition can be considered in the evaluation of L_1 for a variation of the soft inflow boundary conditions.

For the computations of viscous flows, additional viscous conditions are required: The tangential stresses and the normal heat flux have zero spatial gradients in the direction normal to the inflow boundary. The viscous conditions are expressed as

$$\frac{\partial \tau_{xy}}{\partial n} = \frac{\partial \tau_{yz}}{\partial n} = \frac{\partial \tau_{zx}}{\partial n} = \frac{\partial q_n}{\partial n} = 0 \tag{18}$$

where n means the normal direction. These conditions are used to remove unnecessary wave reflections generated by jumps of the viscous flux derivatives at the boundary.

B. Nonreflecting Outflow Conditions

Considering a subsonic exit plane $\xi = \xi_{\max}$ where the nonreflecting boundary conditions are implemented, one can notice that four characteristic waves, L_1, L_2, L_3, and L_4 are leaving the computational domain while L_5 is entering it at the speed of λ_5. Specifying one inviscid boundary condition for the primitive variables would generate reflected waves. For example, imposing the static pressure at the outlet $p = p_\infty$ leads to a well-posed problem, which will, however, create acoustic wave reflections. Therefore, it is necessary to use only nonreflecting boundary conditions to avoid this kind of reflection. The desirable nonreflecting outflow conditions will let the acoustic waves radiate well through the boundary and make the mean flow information in the far field feed back into the computation. Physically, this information is transported by waves reflecting on the regions far from computational domain where some static pressure p_∞ is specified and propagating back from the outside of the domain to the inside through the boundaries. Thus, some physical information on the mean static pressure should be added to the set of outflow boundary conditions so that the problem remains well posed.[6]

One possible physical condition is chosen for the outflow boundary condition, that is, the pressure at infinity, is imposed. This condition does not fix any of the dependent variables and all conservation equations in the system of Eq. (6) are solved on the boundary. This condition is now used to obtain the amplitude variation of the incoming wave L_5. The other four L_i are computed from interior points using Eq. (7). If the exit pressure is not close to p_∞, reflected waves will enter the domain through the exit boundary to bring the mean exit pressure back to a value close to p_∞. A simple way to ensure a well-posed state is to set the amplitude of incoming wave as

$$L_5 = K_{\mathrm{out}}[(p - p_\infty)/\rho c] \tag{19}$$

where K_{out} is a constant expressed as

$$K_{\mathrm{out}} = \sigma_{\mathrm{out}}\left(1 - M_{\max}^2\right)(c/l) \tag{20}$$

The form of constant K_{out} is the one proposed by Rudy and Strikwerda,[18] who derived a similar boundary condition but applied it only in the energy equation. When $\sigma_{\mathrm{out}} = 0$, Eq. (19) sets the amplitude of reflected waves to 0. This is the case used by Thompson[5] and called a perfectly nonreflecting condition. This condition, however, results in ill-posed effects of the drifting mean pressures in the whole domain after a long-time calculation, as mentioned in Ref. 6. By going through some numerical experiments and tests, Poinsot and Lele[6] found an optimal value of the coefficient $\sigma_{\mathrm{out}} = 0.25$. This value is applied to actual computations here as well. In this way, all amplitudes of the characteristic waves are determined, and the results are inserted in Eq. (8) to impose the nonreflecting outflow conditions on the normal-flux derivative terms of Eq. (6). For the computations of viscous flows, additional viscous conditions are required, which are the same as those for the soft inflow conditions as expressed by Eq. (18).

C. No-Slip Wall Conditions

Considering a no-slip wall plane $\xi = \xi_{\max}$, all velocity components vanish at the wall, and, therefore, the wave amplitudes L_1, L_2, and L_3 become zero from Eq. (4) in which the wave speeds λ_1, λ_2, and λ_3 are equal to U. One wave L_4 is leaving the computational domain through the wall, while a reflected wave L_5 is entering the domain. LODI relation (13) suggests that the amplitude of the reflected wave should be

$$L_5 = L_4 \tag{21}$$

where L_4 is computed from interior points using Eq. (7). Now, all amplitudes of the characteristic waves are determined and inserted in Eq. (8) to impose the no-slip wall conditions on the normal-flux derivative terms of Eq. (6). Because all velocity components are fixed by zero values, the momentum equations in the system of Eq. (6) are not needed. The continuity and the energy equations are solved to obtain density and pressure. When an adiabatic wall is considered, the normal heat flux is set to be zero on the boundary:

$$q_n = 0 \tag{22}$$

where n means the direction normal to the solid wall boundary.

IV. Application to Actual Computation

A. Numerical Schemes and Problem Definition

The generalized characteristic boundary conditions are applied to actual computation of Navier–Stokes equations using the high-order and high-resolution numerical algorithms. For the present work, the optimized fourth-order compact (OFOC) schemes are used for the evaluation of spatial derivatives and the fourth-order Runge–Kutta scheme is used for the integration in time.[1,19,20] The viscous terms are differenced twice in succession using the OFOC schemes for the first-order derivatives. Two-dimensional laminar flow over a circular cylinder is computed, and von Kármán vortex streets behind the cylinder are simulated. Oscillating lift and drag force on the cylinder surface are calculated, and the far-field acoustic sound induced by the regular shedding of vortices, which is well known as the dipole Aeolian tone sound, is measured directly. The Reynolds number $Re_\infty = 400$ based on the free-stream velocity and the cylinder diameter and the freestream Mach number $M_\infty = 0.3$ are imposed on the computation. In the literature, it was shown that the streets of regularly spaced vortices exist with laminar cores over the range of Reynolds numbers from 65 to approximately 400. It can be considered that the flow is laminar on the whole in the present computation.

B. Grid Mesh and Computation Procedure

The grid meshes are clustered on the cylinder surface and the downstream region, where large gradients and variations of flow properties exist. These are generated by combining some kind of algebraic functions of second-order continuities, and the grid metrics are evaluated exactly. There is no error caused by the grid metrics in this computation. The computational domain and grid system are shown in Fig. 1. The numbers of grid points are 201 in circumferential direction and 101 in radial direction (201×101). The grid points are so concentrated near the cylinder surface that the boundary layer can be captured by about 20 points on an average in the radial direction. The minimum grid size at the rear side of cylinder surface is given as $\Delta x/d = 0.005$ and $\Delta y/d = 0.02$, where d is the cylinder diameter. The diameter of the far-field circle is 40 times as long as the cylinder diameter. This domain size is determined to capture at least one wavelength of the dipole sound waves in the radial direction, in the aeroacoustic sense. The soft inflow conditions are implemented on the left-half circle plane, the nonreflecting outflow conditions on the right-half circle plane, and the no-slip wall conditions on the cylinder surface in Fig. 1. The computation is continued until the nondimensional time reaches $t^* = tu_\infty/d = 223.2$, where u_∞ is the inflow speed, and about 72 vortices have been shed from the upper and lower surface of the cylinder alternatively during that time. The size of time step is determined by Courant–Friedrichs–Lewy condition of Courant number 0.9, and there 250,000 time steps at the final stage.

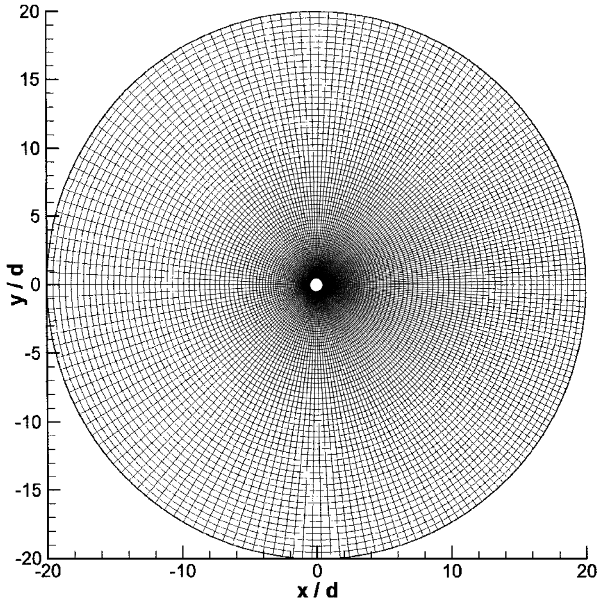

Fig. 1 Grid mesh system for computation of circular cylinder flow.

C. Overview of Sound Generation and Propagation

As the results of the computation, the density and the Mach number contours that cannot be provided by the incompressible flow computations are presented to visualize the effects of compressibility in Figs. 2 and 3, respectively. The density contour plots show the propagation pattern of far-field acoustic waves generated by the shedding vortices behind cylinder and reveal the position of each vortex clearly. The Mach number contours show the attached boundary layer on the front surface of the cylinder, the mixing layers of the separated flows, and the downstream flow patterns well. By the direct computation of compressible flow, the generation and propagation of acoustic waves, which come from the close relations between the fluctuations of density, pressure, and velocity, are simulated well, where the fluctuation magnitudes in the far field are much smaller than those in the near field by three to four orders.

The effect of compressibility in the near field causes the variations of density as well as the pressure and velocity in space and time, and eventually these generate the acoustic waves propagated to the far field, where the flow is almost incompressible. In Fig. 2b, just behind the cylinder, a pair of vortices rotating in reverse directions with each other create an induced velocity in the direction upstream to the cylinder. The induced velocity conflicts with the cylinder surface, and a high-density spot is produced there. This spot is located just above or below the nearest vortex from the cylinder. The high-density spot and the nearest vortex having a low-density spot on its center construct a dipole source whose direction is oscillating up and down as the vortices are shedding from the upper and the lower surfaces of the cylinder. This phenomenon makes the Aeolian tone sound of cylinder flows. The resulting sound pressure fields are shown in Fig. 4, where the typical dipole acoustic fields are represented clearly. The soft inflow conditions are so effective in this case that no reflections are made at the inlet boundary, that is, left-half circle plane. Otherwise, unwanted serious reflections would be generated if the earlier inflow conditions were implemented, as mentioned in the Introduction and Sec. III.A. The sound field made by Poinsot and Lele's inflow conditions[6] is shown in Fig. 5, where

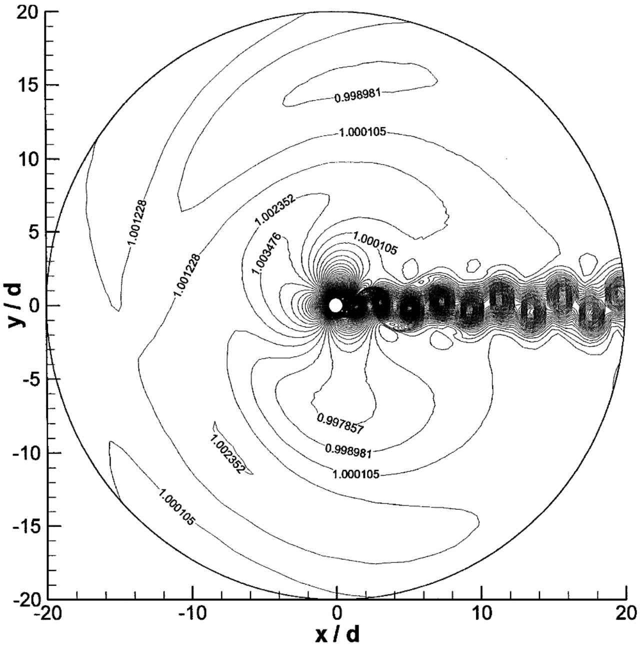

a) Entire view (151 levels)

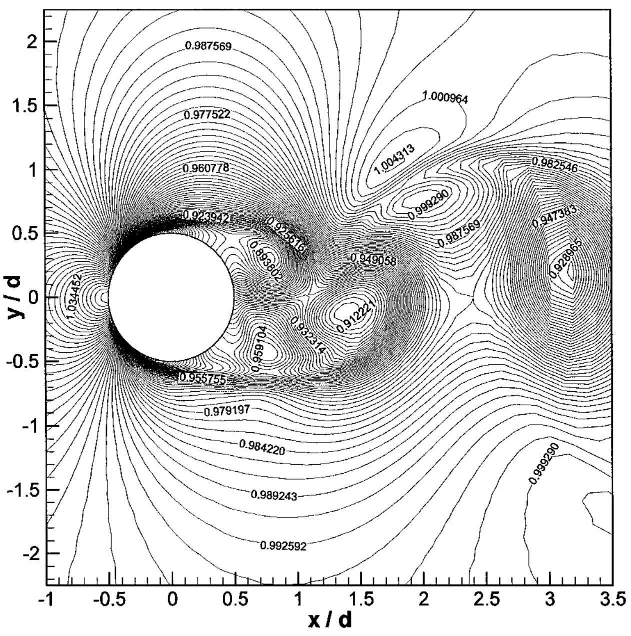

b) Zoomed view (101 levels)

Fig. 2 Density contours (ρ/ρ_∞) at the final stage.

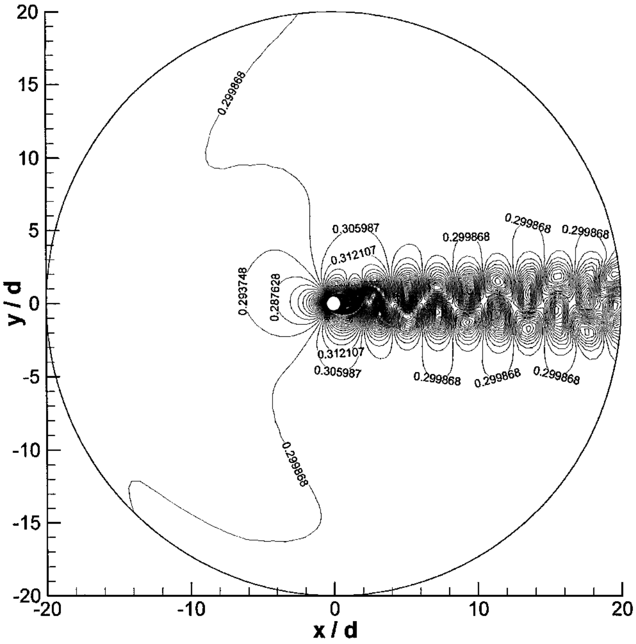

Entire view (76 levels)

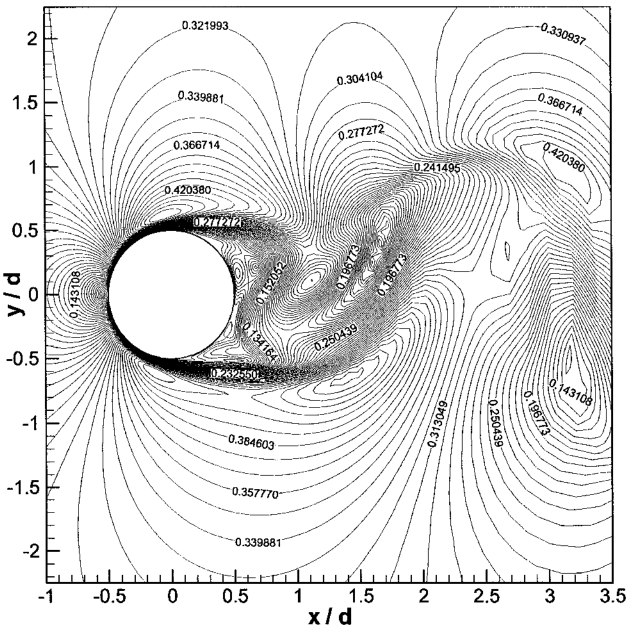

Zoomed view (51 levels)

Fig. 3 Mach number contours at the final stage.

it is obvious that the reflected waves contaminate the whole sound field.

D. Aerodynamic Results vs Experimental Data

The lift and the drag force exerted on the cylinder surface fluctuate in time due to the periodic shedding of vortices. The frequency or period of vortex shedding can be measured by evaluating those of the oscillating lift or drag coefficient. Time-dependent signals of lift and drag coefficient are presented in Fig. 6, where the lift and the drag coefficient are calculated by integrating the distributions of pressure and shear stresses on the cylinder surface. Because the computation begins with an impulsive initial condition that is given by the potential flow solutions, vortex shedding does not occur for a considerable time. However, after the first shedding occurs, the flow goes through a transient state to arrive at the state of periodic shedding of vortices, as shown in Fig 6. It is obvious that a constant frequency and magnitude of fluctuations are acquired in the periodic shedding mode. The Strouhal number calculated by the results in Fig. 6 is $St = f_s d/u_\infty = 0.211$, where f_s is the shedding frequency. Moreover, the rms lift and the mean drag coefficient are also calculated with the results in Fig. 6 as $\overline{C_L^2}^{1/2} = 0.711$ and $\overline{C_D} = 1.163$.

In a regular range of Reynolds numbers from about 6×10^1 to 5×10^3, experimental measurements show that the nondimensional frequency of shedding vortices, that is, the Strouhal number, depends only on Reynolds number. According to Refs. 21 and 22, most measurements reveal Strouhal numbers of 0.21 ± 0.005 and the mean drag coefficients of 1.17 ± 0.01 where $Re_\infty = 400$. Therefore, the Strouhal number and the mean drag coefficient calculated in the present computation are in very good agreement with the experimental measurements performed in Refs. 21 and 22. The value of rms lift coefficient calculated in this paper then can be proposed as an accurate result. By the comparisons between the computation results and the experimental data, it is concluded that the generalized characteristic boundary conditions are used accurately at the wall.

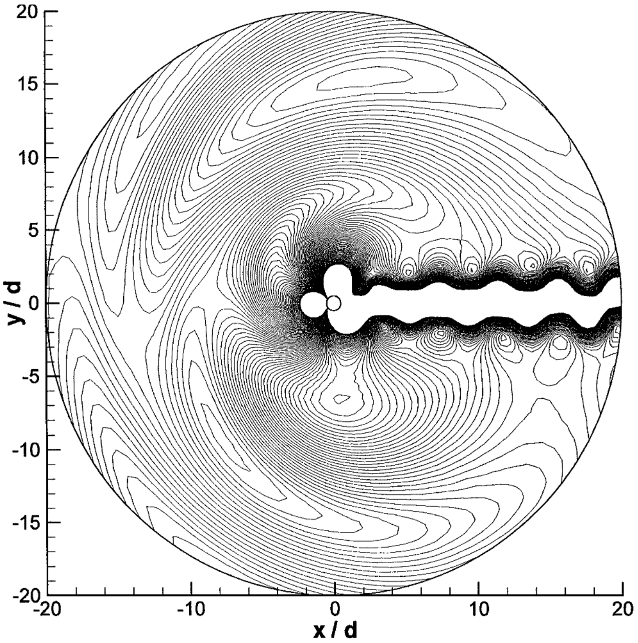

Fig. 4 Visualization of dipole sound field: pressure contours (p/p_∞) filtered for acoustic waves at the final state (101 levels).

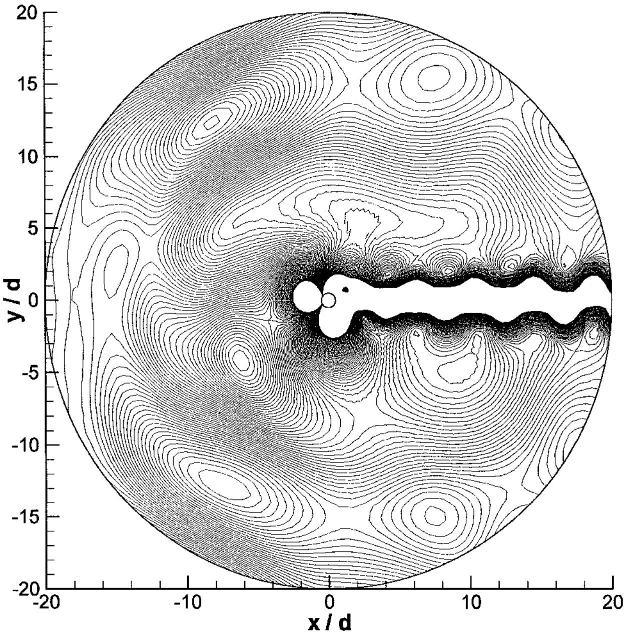

Fig. 5 Contaminated sound field due to the earlier reflective inflow conditions.

E. Aeroacoustic Results vs Analytic Estimations

Acoustic waves generated by the periodic shedding of vortices are measured at the far-field boundary. The Aeolian tone sound radiated by the flow across a circular cylinder is one of the most fundamental of acoustic phenomena. It is a kind of dipole sound generated by nonvibrating bodies. This sound is measured directly in the present computation without solving an integral equation of acoustic analogy. The measurement of acoustic waves is performed at three points of the far-field boundary: *a*, front end; *b*, upper end; and *c*, lower end. Time-dependent signals of acoustic pressure are presented in Fig. 7. The sound pressure levels (SPL) at the three points calculated by the results in Fig. 7 are $\overline{p'^2}^{1/2}/p_\infty = 1.709 \times 10^{-4}$ (118.6 dB), 1.277×10^{-3} (136.1 dB), and 1.278×10^{-3} (136.1 dB) at point *a*, *b*, and *c*, respectively. These fluctuation values are relatively small (less than the mean value by three to four orders of magnitude) so that the standard numerical schemes and nonphysical boundary conditions cannot reproduce them precisely for this problem.

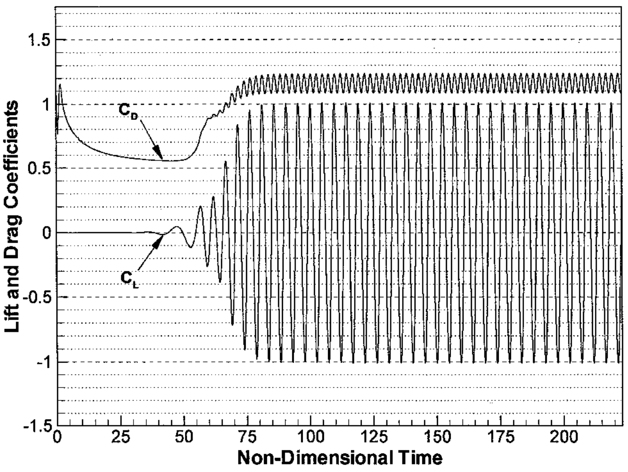

Fig. 6 Time-dependent signals of lift and drag coefficient.

The radiated SPL from any two-dimensional compact rigid body can be estimated by an analytic formula, which is directly proportional to the rms fluctuating force per unit length on the body surface, so that

$$\overline{p'^2}^{\frac{1}{2}}(\boldsymbol{x}) = \tfrac{1}{2}\sqrt{\omega/2\pi r c_\infty}\,\overline{F^2(t)}^{\frac{1}{2}}\cos\theta \tag{23}$$

where θ is measured from the direction of the fluctuating force vector.[21] The fluctuating forces include the lift and the drag force. This equation does not contain the effects of quadrupole sources, and it is applicable to subsonic range in which the quadrupole strength is negligible in comparison to the dipole. Then the SPL at the far-field boundary can be estimated analytically by the following relation:

$$\frac{\overline{p'^2}^{\frac{1}{2}}(\boldsymbol{x})}{p_\infty} = \frac{\rho_\infty u_\infty^2 A}{4p_\infty}\sqrt{\frac{\omega}{2\pi r c_\infty}}\Big[\overline{C_L^2}\cos^2\theta + 4\overline{(C_D - \overline{C_D})^2}\sin^2\theta\Big]^{\frac{1}{2}} \tag{24}$$

where the present values of Strouhal number 0.211, rms lift coefficient 0.711, and the mean drag coefficient 1.163 are used. From Eq. (24), the analytic estimations of SPL at the three points are $\overline{p'^2}^{1/2}/p_\infty = 1.890 \times 10^{-4}$ (119.5 dB), 1.260×10^{-3} (136.0 dB), and 1.260×10^{-3} (136.0 dB) at point *a*, *b*, and *c*, respectively. Therefore, it is shown that the SPL computed directly in the present work are in good agreement with those estimated analytically by Eq. (24) with a tolerable accuracy. The differences between the SPL obtained by the direct computation and by the analytic formula are less than 1 dB. Also, the directivity patterns of the far-field SPL obtained by the direct computation and by Eq. (24) are plotted in Fig. 8 to reveal the accurate results of the present work at all angles on the whole, except for the wake region. In these comparisons between the computation results and the analytical estimations, it is concluded that the generalized characteristic boundary conditions are used accurately at the inlet and the exit plane.

F. Miscellaneous Test

Grid convergence of the present computations is tested to support the accuracy obtained in the preceding results and to show the robustness of the numerical algorithms used and the boundary conditions developed. The same computations are done on four other grid meshes (181 ×91, 161 ×81, 141 ×71, and 121 ×61), which are coarser than the original grid meshes (201 ×101) used earlier. The results of grid convergence study are given in Table 1, where the Strouhal number, the rms lift coefficient, the mean drag coefficient, and the far-field SPL at the three observer points are listed according to the five kinds of grid meshes and are compared with the experimental data or the analytic estimations. The grid convergence test reveals that the results of original computation have little grid dependency and their accuracy is verified sufficiently.

Table 1 Comparison of the results on various grid meshes for grid convergence study

Case	St	$\overline{C_L^2}^{1/2}$	$\overline{C_D}$	$\overline{p_a'^2}^{1/2}/p_\infty$	$\overline{p_b'^2}^{1/2}/p_\infty$	$\overline{p_c'^2}^{1/2}/p_\infty$
Experimental or analytic	0.21 ± 0.005	——	1.17 ± 0.01	1.890×10^{-4} (119.5 dB)	1.260×10^{-3} (136.0 dB)	1.260×10^{-3} (136.0 dB)
Grid 1 (201 × 101)	0.211	0.711	1.163	1.709×10^{-4} (118.6 dB)	1.277×10^{-3} (136.1 dB)	1.278×10^{-3} (136.1 dB)
Grid 2 (181 × 91)	0.210	0.707	1.158	1.686×10^{-4} (118.5 dB)	1.264×10^{-3} (136.0 dB)	1.265×10^{-3} (136.0 dB)
Grid 3 (161 × 81)	0.206	0.687	1.138	1.534×10^{-4} (117.7 dB)	1.241×10^{-3} (135.9 dB)	1.240×10^{-3} (135.9 dB)
Grid 4 (141 × 71)	0.201	0.649	1.099	1.330×10^{-4} (116.5 dB)	1.202×10^{-3} (135.6 dB)	1.203×10^{-3} (135.6 dB)
Grid 5 (121 × 61)	0.195	0.605	1.058	0.970×10^{-4} (113.7 dB)	1.082×10^{-3} (134.7 dB)	1.082×10^{-3} (134.7 dB)

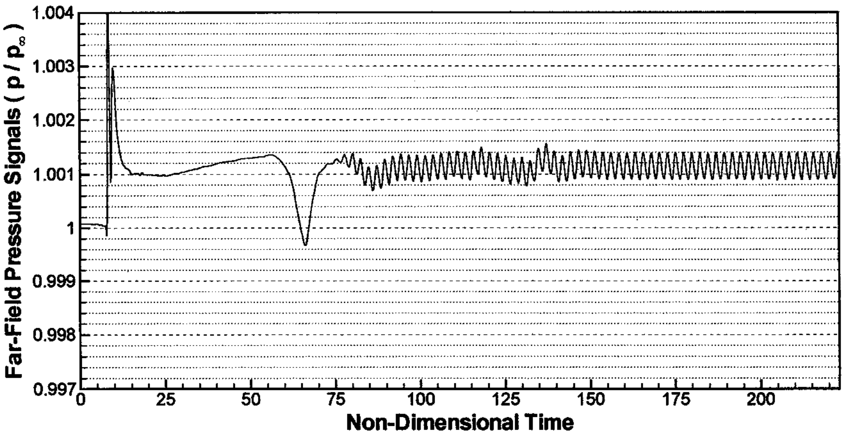

At the front end

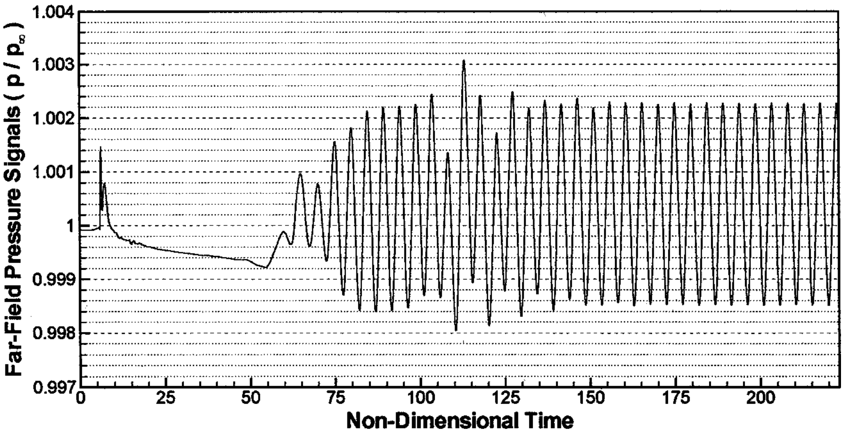

At the upper end

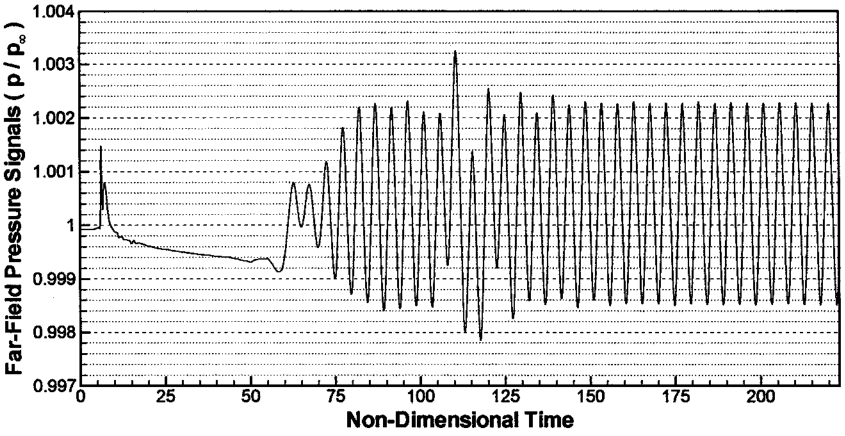

At the lower end

Fig. 7 Acoustic signals of the far-field boundary.

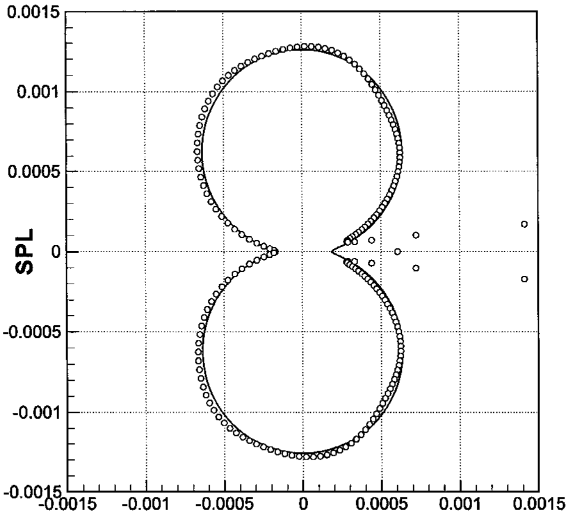

Fig. 8 Directivity pattern of the overall SPLs obtained by the direct computation (○) and analytic estimation (——).

V. Conclusions

The generalized characteristic boundary conditions for the entire conservation-form Euler or Navier–Stokes equations are formulated and applied successfully. The soft inflow conditions are implemented so effectively as to accomplish the nonreflecting features and maintain the mean inflow velocity at the inlet boundary. The improved boundary conditions are used well with the high-order and high-resolution schemes to solve the flow and the acoustic field accurately at the same time, in the presence of a solid body in the flow. The extended formalism derived in the generalized coordinates and the results of its applications verified by the experimental data and the analytic estimations are used for the further developments of CAA research with the characteristic boundary conditions.

Acknowledgment

The authors would like to acknowledge the high-performance computer services from the Supercomputing Center of the Korea Research and Development Information Center.

References

[1] Kim, J. W., and Lee, D. J., “Implementation of Boundary Conditions for Optimized High-Order Compact Schemes,” *Journal of Computational Acoustics*, Vol. 5, No. 2, 1997, pp. 177–191.

[2] Hixon, R., Shih, S. H., and Mankbadi, R. R., “Evaluation of Boundary Conditions for Computational Aeroacoustics,” *AIAA Journal*, Vol. 33, No. 11, 1995, pp. 2006–2012.

[3] Givoli, D., “Non-Reflecting Boundary Conditions,” *Journal of Computational Physics*, Vol. 94, No. 1, 1991, pp. 1–29.

[4] Thompson, K. W., “Time Dependent Boundary Conditions for Hyperbolic Systems,” *Journal of Computational Physics*, Vol. 68, No. 1, 1987, pp. 1–24.

[5] Thompson, K. W., “Time Dependent Boundary Conditions for Hyperbolic Systems II,” *Journal of Computational Physics*, Vol. 89, No. 2, 1990, pp. 439–461.

[6] Poinsot, T. J., and Lele, S. K., “Boundary Conditions for Direct Simulations of Compressible Viscous Flow,” *Journal of Computational Physics*, Vol. 101, No. 1, 1992, pp. 104–129.

[7] Giles, M. B., “Nonreflecting Boundary Conditions for Euler Equation Calculations,” *AIAA Journal*, Vol. 28, No. 12, 1990, pp. 2050–2058.

[8] Tam, C. K. W., and Webb, J. C., “Dispersion-Relation-Preserving Finite Difference Schemes for Computational Acoustics,” *Journal of Computational Physics*, Vol. 107, No. 2, 1993, pp. 262–281.

[9] Bayliss, A., and Turkel, E., “Far Field Boundary Conditions for Compressible Flows,” *Journal of Computational Physics*, Vol. 48, No. 1, 1982, pp. 182–199.

[10] Hagstrom, T., and Haraharan, S. I., “Accurate Boundary Conditions for Exterior Problems in Gas Dynamics,” *Mathematics of Computation*, Vol. 51, No. 184, 1988, pp. 581–597.

[11] Berenger, J. P., “A Perfect Matched Layer for the Absorption of Electromagnetic Waves,” *Journal of Computational Physics*, Vol. 114, No. 2, 1994, pp. 185–200.

[12] Hu, F. Q., “On Absorbing Boundary Conditions for Linearized Euler Equations by a Perfectly Matched Layer,” *Journal of Computational Physics*, Vol. 129, No. 1, 1996, pp. 201–219.

[13] Tsynkov, S. V., “Numerical Solution of Problems on Unbounded Domains,” *Applied Numerical Mathematics*, Vol. 27, No. 4, 1998, pp. 465–532.

[14] Tourrette, L., “Artificial Boundary Conditions for the Linearized Compressible Navier–Stokes Equations,” *Journal of Computational Physics*, Vol. 137, No. 1, 1997, pp. 1–37.

[15] Lockhard, D. P., and Morris, P. J., “Radiated Noise from Airfoils in Realistic Mean Flows,” *AIAA Journal*, Vol. 36, No. 6, 1998, pp. 907–914.

[16] Hirsch, C., “The Mathematical Formulation of the System of Euler Equations,” *Numerical Computation of Internal and External Flows*, 1st ed., Vol. 2, Wiley, New York, 1992, pp. 132–223.

[17] Warming, R. F., Beam, R. M., and Hyett, B. J., “Diagonalization and Simultaneous Symmetrization of Gas-Dynamic Matrices,” *Mathematics of Computation*, Vol. 29, No. 132, 1975, pp. 1037–1045.

[18] Rudy, D. H., and Strikwerda, J. C., “A Nonreflecting Outflow Boundary Conditions for Subsonic Navier–Stokes Calculations,” *Journal of Computational Physics*, Vol. 36, No. 1, 1980, pp. 55–70.

[19] Kim, J. W., and Lee, D. J., “Optimized Compact Finite Difference Schemes with Maximum Resolution,” *AIAA Journal*, Vol. 34, No. 5, 1996, pp. 887–893.

[20] Kim, J. W., and Lee, D. J., “Numerical Simulation of Nonlinear Waves Using Optimized High-Order Compact Schemes,” *Computational Fluid Dynamics Journal*, Vol. 5, No. 3, 1996, pp. 281–300.

[21] Blake, W. K., “Dipole Sound from Cylinders,” *Mechanics of Flow-Induced Sound and Vibration*, 1st ed., Vol. 1, Academic Press, New York, 1986, pp. 219–287.

[22] Schlichting, H., “Outline of Boundary-Layer Theory,” *Boundary Layer Theory*, 7th ed., McGraw–Hill, New York, 1979, pp. 24–46.

P. J. Morris
Associate Editor